Noncontact Measurement of Density and Thermal Properties of SS 316L Powder Bed through Flash Thermography

Abstract

Purpose – Powder bed density is a key parameter in powder bed additive manufacturing (AM) processes but is not easily monitored. This research evaluates the possibility of non-invasively estimating the density of an AM powder bed via its thermal properties measured using flash thermography (FT).

Design/methodology/approach - The thermal diffusivity and conductivity of the samples were found by fitting an analytical model to the measured surface temperature after flash of the powder on a polymer substrate, enabling the estimation of the powder bed density.

Findings – FT estimated powder bed was within 8% of weight-based density measurements and the inferred thermal properties are consistent with literature findings. However, multiple flashes were necessary to ensure precise measurements due to noise in the experimental data and the similarity of thermal properties between the powder and substrate.

Originality/Value – This paper emphasizes the capability of Flash Thermography (FT) for non-contact measurement of SS 316L powder bed density, offering a pathway to in-situ monitoring for powder bed AM methods including binder jetting (BJ) and powder bed fusion. Despite the limitations of the current approach, the density knowledge and thermal properties measurements have the potential to enhance process development and thermal modeling powder bed AM processes, aiding in understanding the powder packing and thermal behavior .

Keyword BJ printing, Powder bed, Flash Thermography, Powder bed density, non-contact measurement, Thermal measurement, SS 316L powder

Paper type Research paper

Introduction

Additive manufacturing (AM) fabricates items layer-by-layer from a digital model. Powder Bed Fusion (PBF) and Binder Jetting (BJ) are AM technologies that utilize powder beds. PBF utilizes a laser or other energy beam to fuse powder particles layer by layer in the desired region (Kruth et al., 2005). BJ prints droplets of binding agent to join powder particles. BJ parts typically require post-processing by sintering or infiltration to attain the final mechanical properties (Ziaee and Crane, 2019, Farzadi et al., 2014, Gaytan et al., 2015, Technologies and Terminology, 2012). Because BJ deposits a liquid agent to bond the powder particles, unprinted powder is referred to as dry powder. While the post-processing is a slow batch process, BJ builds at higher rates and processes materials that are hard for other AM techniques, such as high melting point or high reflectivity materials (Miyanaji et al., 2020).

The quality of the spread powder layer is important in both PBF and BJ, but it is particularly

critical in BJ (Liu et al., 2011, Utela et al., 2008). In BJ, powder bed density strongly influences the mechanical properties of the final part. Increasing the powder bed density leads to a rise in the green body density which reduces shrinkage during sintering and enhances mechanical properties of the final part (Utela et al., 2008, Mostafaei et al., 2021, Li et al., 2020, Ziaee and Crane, 2019, Wheat et al., 2018). Therefore, the powder bed density is generally maximized. Slower spreading velocity, thinner layers, and a counter-rotating roller can increase the powder bed density (Haeri et al., 2017, Chen et al., 2017, Ali et al., 2018). The powder bed density is also affected by the location in the powder bed—especially when using a feed piston. Ali et al. measured a 21.1% decrease in the powder bed density along the rolling direction (Ali et al., 2018, Solutions, 2014).

Current powder bed density measurement techniques, such as printed cups and the plug method, require large powder volumes and disturb the powder bed, meaning that the density can only be measured after printing and with low resolution (Elliott et al., 2016, Ziaee et al., 2017). If powder bed density varies during the manufacturing process, the flaws will not be detected until the printing and/or post-processing are finished. This will increase both cost and time. A non-contact method for measuring powder bed density would address this problem. Flash thermography (FT) is a potential solution to monitor the powder bed density without disturbing the powder. This method could also provide valuable insight into the thermal properties of the powder bed which impact binder drying/curing in BJ and cooling in PBF.

FT applies a short thermal pulse onto the sample surface. The change in surface temperature over time is recorded by infra-red (IR) camera. FT can evaluate depth and size of defects, coating thickness, or thermal properties in almost any material including polymers, composites, and steel, and thermally sprayed coatings (Wysocka-Fotek et al., 2012, Muzika et al., 2021, Sun, 2014, Zheng et al., 2015, Rajic, 2013). FT methods are divided based on the number of material layers (strata) assumed in the model where each stratum refers to a region of material that has the same thermal properties.

In a one-stratum system, the bottom is treated as insulated as shown in Figure 1(a). The temperature response can be used to solve for the thermal diffusivity if the thickness is known and vice versa (Sun, 2006). The method thus detects defects below the surface and measure their depth, because the defects act as an insulated boundary. The ratio of defect width to depth should generally be larger than one (Wysocka-Fotek et al., 2012, Wallace et al., 2022). While the pulse is generally treated as instantaneous, longer pulses can be used with appropriate adjustments (Pierce and Crane, 2019).

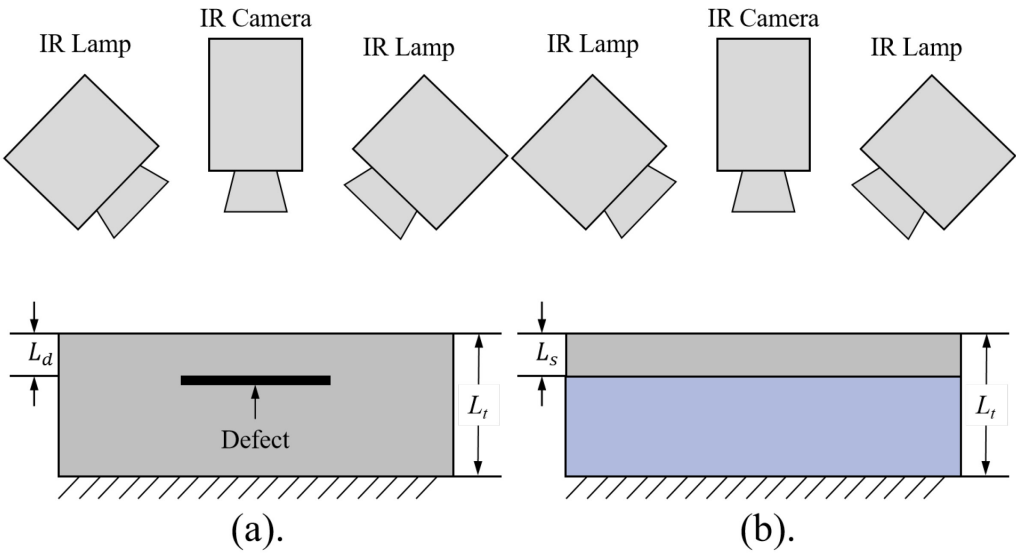

Figure 1. The schematic of FT testing on (a) a one-stratum-system sample and (b) a two-strata system. L_t refers to the total thickness of the sample. L_d is the depth of the defect. L_s means the thickness of the first stratum.

The thermal diffusivity can be determined for a known thickness by the characteristic time of either: 1) the temperature contrast (difference between regions with and without defects) after flash, or 2) the sample's post-flash surface temperature (Parker et al., 1961, Deemer, 1999, Ringermacher et al., 1998, Han et al., 1996, Maldague, 1996, Shepard et al., 2003). Fitting an analytical or numerical solution of the surface temperature after flash to the experimental surface temperature can improve accuracy (Sun, 2003). However, the density of the sample cannot be obtained by the one-stratum sample system, because only thermal diffusivity can be found.

Balagaes found that for a two-strata FT system (Figure 1(b)) with its bottom insulated, the shape of the surface temperature after flash is a function of E (ratio of thermal effusivity) and η as shown in Eq. (1) and Eq. (2) (Balageas et al., 1986).

$$E = \frac{\sqrt{\rho_2 c p_2 k_2}}{\sqrt{\rho_1 c p_1 k_1}} \quad \text{Eq. (1)}$$

$$\eta = \frac{L_s}{L_d} \cdot \sqrt{\frac{\alpha_2}{\alpha_1}} \quad \text{Eq. (2)}$$

In Eq. (1), ρ is density, c_p is specific heat, k is thermal conductivity, and α is thermal diffusivity. Subscripts 1 and 2 represent the first and second stratum respectively. Shepard and Beemer (Shepard and Beemer, 2016) showed that for a semi-infinite two-strata system, the surface temperature after a flash is a function of E. Both thermal diffusivity and thermal conductivity of the top stratum for a semi-infinite two-strata system can be found if four things are known: the thickness of the first stratum and both the thermal diffusivity and the thermal conductivity of the bottom stratum.

Various methods have been proposed for finding E and η from the temperature profile. Sun (Sun, 2010) used a numerical solution pool to enact the least square fitting over the experimental surface temperature data to obtain the thermal conductivity and thermal diffusivity of a stratum. El Rassy employed the least square fitting method based on the semi-analytical solution of the sample system to determine the orthotropic thermal properties through laser FT (El Rassy, 2019). These approaches can find the thermal diffusivity and thermal conductivity of the top stratum of a semi-infinite two-strata system. If the specific heat is known, the density of the stratum can also be

determined using Eq. (1). However, no previous work has been done to extract the density of powder using FT. Powder has much lower thermal conductivity than bulk and introduces additional complications such as rough surface and unknown absorption depths. Therefore, it is necessary to investigate the use of FT to measure the density of powder.

This study investigates the use of FT to non-invasively measure powder bed density in AM processes such as BJ and PBF by measuring the thermal diffusivity and conductivity. To achieve this goal, an analytical solution for the surface temperature over time is developed. The equation is fit to the experimental surface temperature data by adjusting the unknown material properties. This solution is verified using a numerical model created in COMSOL, which is also used to study the fitting range of the least square fitting. The ability of this approach to estimate properties is assessed and the methods for identifying a reliable solution are presented.

Methods and Materials

This section presents the procedure by which the data was analyzed to solve for the thermal properties and density of the top stratum. The analytical model and numerical model are described and validated. Then, the experimental methods are presented.

Model for Flash Thermography

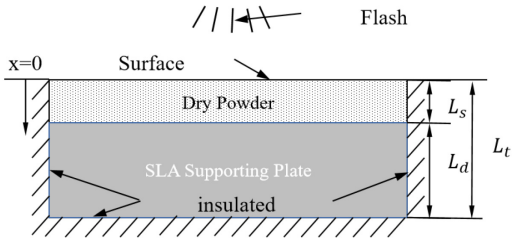

Figure 2. The schematic of the sample and its related assumptions and boundary condition. x refers to the thickness direction of the sample.

The sample is modeled as a 1D system with two homogeneous strata, with no thermal contact resistance ($R_{tc} = 0$) between them as illustrated in Figure 2. The top stratum is SS316L dry powder deposited and rolled by ExOne Innovent BJ printer resting on a plastic supporting plate printed by a stereolithography (SLA) printer. The two thicknesses of the dry powder were measured (0.54 mm or 0.79 mm). The thickness of the bottom plastic stratum (L_d) is 20 mm. The heat input from the flash is assumed to be uniform across the surface and the edge losses are neglected, so a 1D heat transfer model is used to describe this two-strata system. The flash heat input is modeled as a surface flux with a square wave of duration 400 μs to match the length of the experimental pulse. All energy of the flash is assumed to be absorbed at the powder surface. The bottom surface is treated as adiabatic with a uniform initial temperature distribution in the sample. Natural convection is also neglected.

Analytical model

The PDE system of the experimental sample shown in Figure 2 is

$$\frac{\partial^2 T_1}{\partial x^2} = \frac{1}{\alpha_1}\frac{\partial T_1}{\partial t} \quad \frac{\partial^2 T_2}{\partial x^2} = \frac{1}{\alpha_2}\frac{\partial T_2}{\partial t} \qquad \text{Eq. (3)}$$

where T refers to the surface temperature of the sample. The boundary conditions (B.C) and initial conditions (I.C) are given by.

$$\text{B.C } x = 0, -k_1\frac{\partial T_1}{\partial x} = P(Heaviside(t) - Heaviside(t - t_f) \qquad \text{Eq. (4)}$$

$$x = L_s,\ T_1 = T_2, k_1\frac{\partial T_1}{\partial x} = k_2\frac{\partial T_2}{\partial x} \qquad \text{Eq. (5)}$$

$$x = L_{t,}\ \frac{\partial T_2}{\partial x} = 0 \qquad \text{Eq. (6)}$$

$$\text{I.C } t = 0, T_1 = T_2 = T_0 \qquad \text{Eq. (7)}$$

where T_0 is the initial temperature before the flash. Subscripts 1 and 2 refer to the top and bottom strata respectively. This PDE system is solved by conjugate integral transformation. The solution of the PDE system is a function of the thicknesses of both strata, α and k of both strata, the flash duration, and the flash magnitude.

Because the effect of air on the specific heat of powder is negligible, the relative density of the sample using FT (f_{FT}) of the sample can be found from the thermal flash measurements if the bulk thermal mass and the thermal properties of the sample are known using,

$$(\rho c_p)_p = \frac{k}{\alpha} \qquad \text{Eq. (8)}$$

$$f_{FT} = \frac{(\rho c_p)_p}{(\rho c_p)_s} \qquad \text{Eq. (9)}$$

In Eq. (8) and Eq. (9), ρc_p refers to the thermal mass (density multiplied by specific heat).

Numerical model

A numerical model was built in COMSOL for validating the analytical solution, studying the optimal fitting range and understanding the impact of measurement noise. The thermal properties used in the model are summarized in Table 1. The dry powder values were obtained from preliminary FT measurements on powder beds with thicknesses of 0.54 mm and 0.79 mm. The thermal properties of the SLA measurement plate (20 mm thick) were obtained by transient plane heat source (TPS) (hot disc) carried out by Tc-Kit (C-Therm, USA). The surface temperature is extracted from COMSOL solution every 0.01 s to match the IR camera data.

Table 1. The thermal properties of 0.54 mm dry powder, 0.79 mm dry powder, and 20 mm SLA measurement plate used in all simulation and model inputs. *E* values of the two sample systems are also shown.

Sample name	**0.54 mm dry powder**	**0.79 mm dry powder**	**SLA measurement plate**
***α* (*10^-7 m^2/s)**	0.8472	0.7797	1.6337
***k* (/10 W/mK)**	1.8572	1.7811	2.3210
Thickness(mm)	0.54	0.79	20
E	0.9000	0.9003	

Least Square Fitting

The analytical solution is a function of the thicknesses of both strata, the α and k of both strata,

the flash duration, and the flash magnitude. Shepard and Beemer (Shepard and Beemer, 2016) showed that for the semi-infinite two strata system (η~0), the surface temperature over time after is only a function of E. Because $L_t > 25L_s$, and the α and k of the printed SLA plastic are relatively small, the sample system studied in this paper can be considered a semi-infinite two strata system.

To obtain α_1 and k_1, it's imperative to know the four parameters of the sample system mentioned in introduction and the flash duration, t_f. The values of α_2 and k_2 (SLA plastic substrate) were quantified utilizing the TPS method as reported in Table 1. The thickness of the dry powder was measured as described below. The flash duration was set as 400 μs. The analytical solution is fit to the experimental surface temperature by finding the values of the α_1, k_1, and the flash magnitude (P) that minimize the least square error between the analytical model and experimental data given by

$$l_{se} = \sum_{n_{st}}^{n_f} (T_{exp}(t(i)) - T_{an}(t(i)))^2 \qquad \text{Eq. (10)}$$

where l_{se} is the least square error, T_{exp} refers to the experimental surface temperature, T_{an} represents the analytical solution of surface temperature, i refers to time the step, n_{st} is the initial time step for fitting, and n_f is the end time step for fitting. The least square fitting is conducted using a gradient-based interior point method in MATLAB™. The selection of starting point and ending point of the fitting are discussed below.

Stage of surface temperature for semi-infinite two strata system

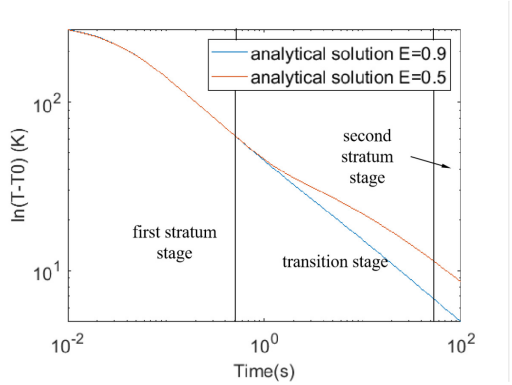

Figure 3. The surface temperature change over time in log scale with E (ratio of thermal effusivity of layer 1 and layer 2) equaling 0.5 and 0.9. The transition stage when E = 0.5 is much more distinct than that of E = 0.9.

The surface temperatures over time for two values of E (0.5 and 0.9) for a two-stratum system are shown in Figure 3. The surface temperature after flash can be divided into three stages: first stratum stage, transition stage, and second stratum stage. In the first, stratum one dominates the thermal response. In the transition stage, the second stratum begins to affect the surface temperature change, and in the second stratum stage, the second stratum thermally dominates. For a homogeneous, semi-infinite surface, where all energy is absorbed at the surface, the analytical solution for the temperature change after a flash is given by:

$$\Delta T = \frac{P}{e\sqrt{\pi t}} \qquad \text{Eq. (11)}$$

$$e = \sqrt{k\rho c_p} \qquad \text{Eq. (12)}$$

where e is termed the thermal effusivity. In the first and third stages, the surface temperature after

flash decreases with a slope of -0.5 in logarithmic scale as seen in Figure 3 (Shepard and Beemer, 2016). When heat reaches the second stratum and the second stratum starts to affect the surface temperature, the surface temperature decline will decrease for a semi-infinite two strata system, if E<1, (E value is around 0.9 for this paper) until the second stratum becomes thermally dominant (temperature decreasing rate recovers to -0.5 in log scale). Since the shape of transition stage is a function of E and the slope is identical before and after, the transition stage imparts uniqueness to the analytical solution. As E approaches unity, the transition stage of E nears a straight line as seen in Figure 3 for E=0.9 compared to E=0.5. The closer E is to one, the more similar the two strata are thermally leading to a less distinct transition stage and a greater fitting challenge. This paper focuses on this difficult limiting condition as E approaches one to better understand the limits of the method.

Experimental Measurements

Sample Preparation

Samples were prepared by depositing powder onto the SLA printed substrate. This was done with an ExOne Innovent+™ BJ printer equipped with a single roller. 316L stainless powder (Sandvik USA) -22 μm powder (d50= 7.58 μm) (SANDVIK, Colton et al., 2021). The process parameters of the BJ printer are listed in Table 2.

Table 2. The process parameters of the BJ printer

Process Parameter	Value	Unit
Recoat Speed	100	mm/sec
Ultrasonic Intensity	75	%
Roller Traverse Speed	3	mm/sec
Roller Rotation Speed	600	rpm
Layer Thickness	40	μm

Samples are prepared using 13 and 19 layers of dry powder on SLA plate. For each type of sample, three samples were prepared and tested.

The gap between the roller and the powder bed plate was filled with dry powder to create a datum that is aligned to the roller axis as shown in Figure 4 (a). The powder bed is lowered 10 to 15 mm, and the SLA substrate is placed on the powder bed. A reference block is placed on the substrate as shown in Figure 4 (b) and the powder bed lowered until the reference block contacts the powder on the outer edge shown in Figure 4 (c). At this point, the SLA substrate is at the same height as the powder on the outer edge and the gap between the roller and the SLA substrate is minimized. The reference block is removed, and the desired number of layers of powder (13 or 19 layers) are deposited onto the sample as shown in Figure 4 (d).

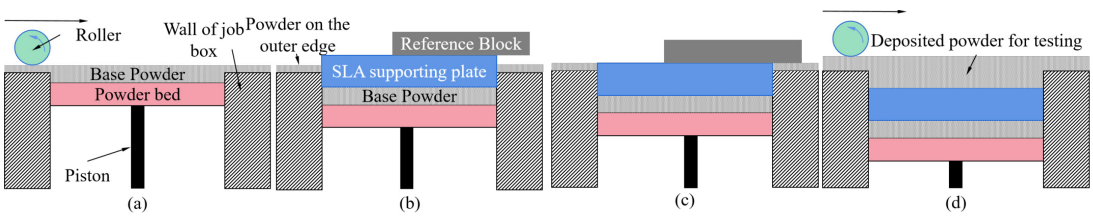

Figure 4. (a) The gap between the powder bed and roller is filled by dry powder.

(b) The SLA supporting plate and reference block are placed on the base powder.

(c) The powder bed lowers until the reference block contacts the powder on the outer edge.

(d) The desired layers of powder are deposited onto the SLA supporting plate.

Including the initial dry powder layer needed to fill the gap between the measuring plate and the roller, the powder thickness of the two types of samples are approximately 0.54 mm and 0.79 mm.

Measurement of Relative Density (f_e)

The f_{FT} is compared to the relative density measured experimentally by the powder weight method (f_e). The experimentally measured value of f_e is defined as

$$f_e = \frac{\rho_p}{\rho_s} \qquad \text{Eq. (13)}$$

where ρ is the density and the subscript p and subscript s refer to the powder form and the solid form, respectively. The density of dry powder (ρ_p) is obtained by.

$$\rho_p = \frac{m_d}{A_m \cdot L_s} \qquad \text{Eq. (14)}$$

where L_s is the thickness of dry powder and A_m is the area of the SLA supporting plate. The dry powder mass, m_d is the difference in mass of the SLA supporting plate with and without powder.

Flash Thermography Setup

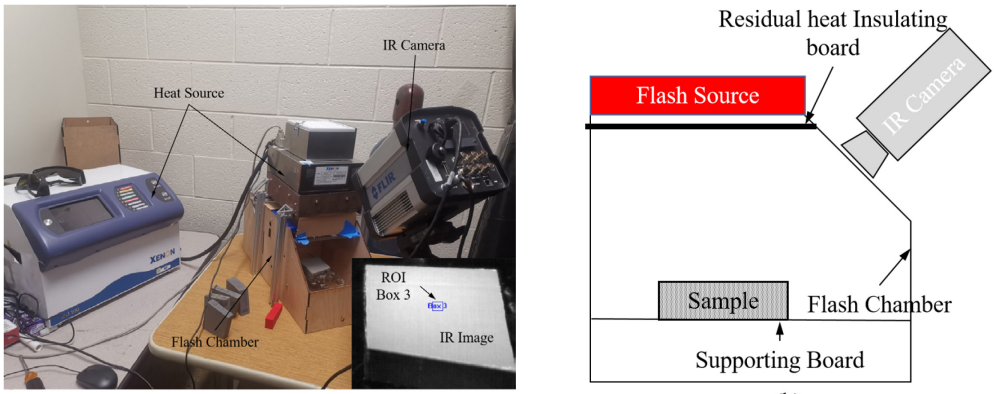

Figure 5. (a). The experimental equipment used for FT. Inset is an IR image of a sample. For specific temperature analysis of designated areas, regions of interest (ROI) are set, as exemplified by the labeled boxes. The average temperature within the ROI is calculated (b). The schematic of the experimental equipment.

The experimental setup of the flash thermography system in this research consists of the heat source, the flash chamber, and the IR camera illustrated in Figure 5. The heat source is a Xenon X-1100 high-intensity pulsed light system with a Xenon LH912 flash lamp which can control flash duration and energy. The flash chamber is a box that supports the sample and the flash lamp. A board slides under the lamp after the flash to prevent the IR radiation emitted from the lamp after the pulse from affecting the surface temperature measurements. Without the board, residual heat from the flash lamp resulted in an increase of f_{FT} of up to 40%. The IR camera is a FLIR SC4000 MWIR

camera with maximum frame rate of 420 Hz at 320x256 resolution. For this work, surface temperature was measured at a frequency of 100 Hz (0.79 mm and 0.54 mm) or 220 Hz (0.54 mm). The experimental temperature is from the region of interest (ROI) at sample center in box 3 as shown in Figure 5 (a). The ROI (Figure 5 (a) box 3) includes approximately 300 pixels. The camera lens is ASIO 50 mm F/2.3 MWIR (JASON TECHNOLOGY INC.).

The six samples were flashed a total of 87 times, with each sample being flashed at least 10 times. A typical experimental cycle is as follows:

1. The Xenon flash source applies a short pulse onto the sample surface. A typical flash has a duration of 400 μs and a total energy of 1067 J.
2. The insulating board is pushed beneath the heat source to block the residual heating, while the IR camera records the surface temperature after flash. Temperature data before 0.5 s is not used in the analysis due to possible residual heating before the insulating board is moved.
3. MATLAB™ is used to fit the analytical solution to the experimental data to find the thermal properties of the dry powder.
4. The sample is cooled for a minimum of 20 min between flashes to ensure the uniform temperature distribution along the thickness direction in the sample as required by Eq. (7).

During the testing procedure, the airflow generated by the cooling fan of the flash lamp and the air conditioning system was eliminated to ensure that the measurement results remain unaffected by active convection.

Noise of IR camera

The temperature data from the IR camera includes noise which impacts the ability to accurately determine the powder properties. In graphs of noise on a logarithmic scale, the noise trend, with a magnitude of 0.01 K, is challenging to discern. The measurement noise (T_d) was estimated from the difference between the experimental surface temperature (T_{exp}) and the analytical solution (T_{fit}) obtained from the least square fitting.

$$T_d(t(i)) = T_{exp}(t(i)) - T_{fit}(t(i)) \qquad \text{Eq. (15)}$$

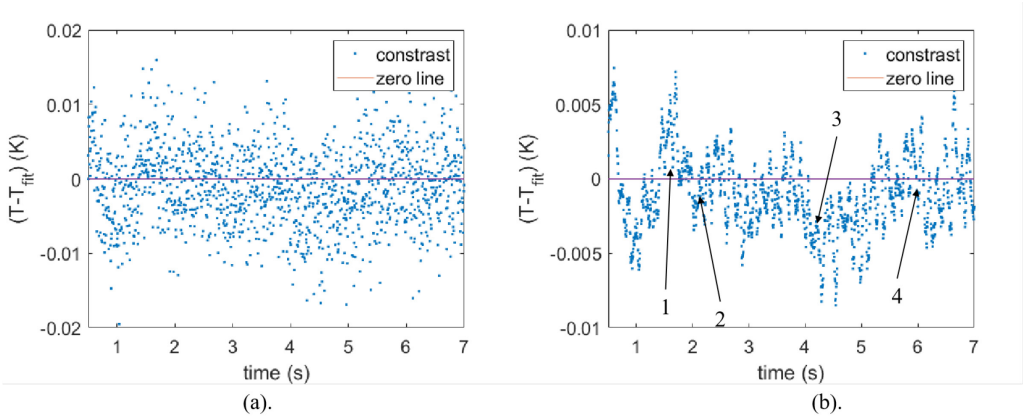

Figure 6. (a). The original $T - T_{fit}$ figure of one flash.

(b). Calculating 11 points moving mean (current point and preceding 10 points) helps identify systemic errors in the noise. Mark 1 and 4 refer to the rise of moving mean. Mark 2 and 3 refer to the drop of moving mean.

Trends in the data points can be seen by computing a moving mean using 11 points (current+10

preceding) as shown in Figure 6. From Figure 6, two types of noise are seen: random noise with a standard deviation of 0.005 K and systemic deviations. Systemic deviations in the temperature are possibly due to the active cooling of the IR camera and small environmental temperature changes. Systemic deviations in the moving mean shift are referred to as residual shift (R_s). Several regions of R_s are marked in Figure 6. When E~0.9, accurate calculation of the sample properties is sensitive to the residual shift as will be discussed below. To highlight the impact of random vs. systemic errors, random noise of the IR camera was measured, and similar normal noise was added into the COMSOL surface temperature to enable separate consideration of random and systemic errors.

Results and Discussion

As the goal of this paper is to validate the methods for conducting the thermal measurements, both the process development and final measurement results are reported in this section.

Random Noise

The numerical COMSOL model was used to verify the accuracy of the analytical solution, study the effect of normal noise of the IR camera signal, and determine the proper fitting time range for the least square fitting. To validate the analytical solution, the analytical solution is fit to the COMSOL temperature data using the Matlab gradient-based method (function: fmincon) to solve for the thermal properties of the powder stratum from 0.5 s to 6t*, where t* is defined as (Shepard and Beemer, 2016)

$$t^* = \frac{L_s^2}{\pi\alpha} \qquad \text{Eq. (16)}$$

Using the thermal properties and thickness provided in Table 1, the t* for the 0.54 mm sample and 0.79 mm sample are 1.10 s and 2.55 s. Figure 7 provides a visual representation of the agreement between the analytical solution, obtained through the least square fitting, and the numerical surface temperature from COMSOL, demonstrating the quality of the fit between the two.

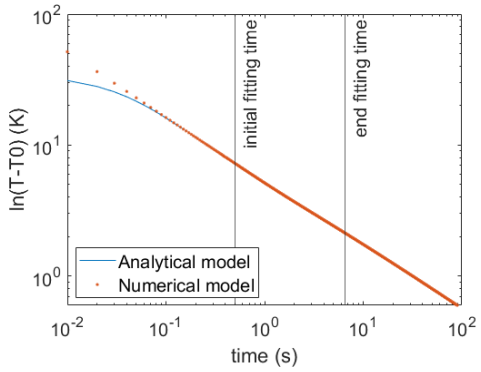

Figure 7. The surface temperature obtained by fitting the analytical solution to the COMSOL simulation of the 0.54 mm geometry. T_0 refers to the surface temperature before flash.

The thermal properties obtained from fitting the analytical solution to the COMSOL surface temperature agree with COMSOL model inputs with less than 1% error. The small difference between the thermal properties from the least square fitting and the input thermal properties may be

due to the arrangement of mesh and computational error.

To study the effect of random camera noise, normally distributed random noise with a standard deviation of 0.005 K was added to the COMSOL calculations of surface temperature. The standard deviation was chosen to match the normal noise determined by analyzing 17 records of the same sample surface temperature in equilibrium condition recorded for two to three seconds at 100 Hz for nine videos and 220 Hz for eight videos. For models of both the 0.54 mm and 0.79 mm samples, the least square fitting was performed 100 times with unique normal-distributed noise generated for each iteration. The results show that in approximately 97.5% of the cases, the error in thermal diffusivity is within $\pm 7.5\%$. Regarding the f_{FT} and thermal conductivity error, 99% of the cases fall within $\pm 5\%$. Thus, even with an E value of 0.9, normal noise does not hinder the effective calculation of thermal properties.

Selecting Fitting Range

The thermal properties extracted from the temperature data depend on the interval over which the analytical model is fit to the data. For the initial data points, the model does not fit well due to some combination of residual heating before the insulation board covers the lamp and some nonuniformity in the energy absorption. However, the difference between the analytical and experimental values are smaller than 0.1 K within 0.5 s of the flash. Numerical experiments showed that the solution was not sensitive to the exact start of the fitting interval. The initial fitting time of 0.5 s was sufficient to exclude the deviations due to nonidealities in the experiment. An optimal end point to fitting is beneficial because a shorter fitting time reduces computational cost and some assumptions such as negligible natural convection may not hold at longer times.

To investigate the minimum end time required for fitting, the surface temperature data from the COMSOL model devoid of normal random noise is utilized. Eliminating the normal noise from the COMSOL surface temperature is essential, as the influence of end fitting time on the R_e of thermal properties is significantly less than that of normal noise. Extending the end fitting time to $3t^*$ reduces all R_e values below 1%. Thus, the minimum end fitting time is $3t^*$. In an experiment condition where thermal diffusivity of the sample is unknown, the t^* based on the calculated thermal diffusivity needs to be smaller than 33% of the end fitting time for the results to be reliable. However, in practice, the minimum end fitting time needs to be bigger than $3t^*$ to reduce the impact of R_s in the experimental data on the measurement results as discussed in the following section.

In actual experiments, the choice of the end fitting time is also dependent on specific patterns of temperature shifts (R_s) that arise in experimental measurements as shown in Figure 8. With E ~0.9, experiments showed that R_s error of ~0.01K near the end of the fitting region impacts the accuracy of the analytical model fit to the experimental data. Therefore, a rise in residual fitting error around 13 s as seen in Figure 8 will not produce a reliable property estimate. This unnatural rise often happens at 13 s to 15 s for 0.54 mm sample and after 20 s for 0.79 mm sample. In addition to measurement errors, this deviation could be partially due to phenomena such as natural convection that begin to impact the accuracy at longer time periods as well.

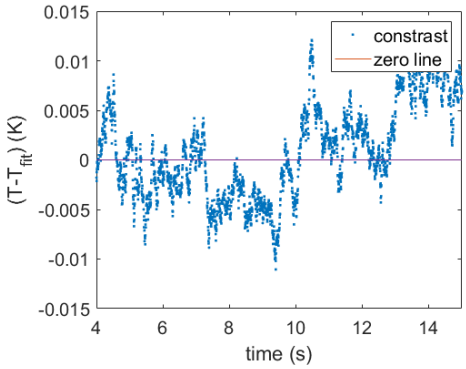

Figure 8. The difference between the fitting model and experimental data for one flash of a 0.54 mm sample. After around 13 s, there is a permanent rise of the experimental data leading to errors in fitting the analytical model.

For each flash of a sample, the analytical model was fit at integer time values within these fitting ranges from 7-15 s for the 0.54 mm samples and 10-21 s for the 0.79 mm samples. Thus, a distinct set of property estimates is derived for multiple end fitting times within the range. After analyzing measurement results from all 87 flashes across the six samples, we established criteria to discern which measurements, from each individual end fitting time of every flash, are acceptable. Measurements not meeting these criteria were discarded. The valid results from the accepted end fitting times for a specific flash are then averaged to produce a single representative value for that flash. This detailed process was consistently applied to all end fitting times across the 87 flashes for all samples. The acceptance criteria are discussed below.

Acceptance Criteria

Due to the presence of R_s, not all fits of the analytical model to the experimental data can obtain thermal properties that provide acceptable f_{FT} measurements that are close to f_e. Therefore, it is critical that standards be established to identify acceptable observations. Acceptance criteria were established to identify acceptable results by observing the $T - T_{fit}$ data of the 89 flashes of the six samples. The acceptance criteria are ordered based on the frequency of their use.

(1) The residual temperature error $T - T_{fit}$ data needs to be distributed around the zero over at least 50% of the $1t^*$ to $4t^*$ time interval. The transition region can be estimated as t^* to $4t^*$ based on the calculated properties. A good property prediction is only possible if the residual temperature error is centered around zero. Figure 9 shows the $T - T_{fit}$ data of the same flash with end fitting time at 10 s and 12 s for one 0.79 mm sample.

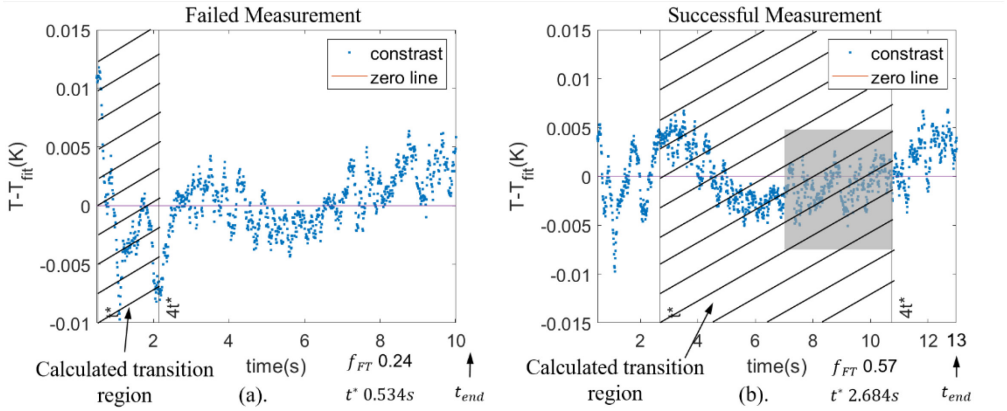

Figure 9. The $T - T_{fit}$ of same flash of one 0.79 mm under different end fitting times, 10 s (a) and 13 s (b). t_{end} is end fitting time. The f_{FT} and t^* at the end fitting time is displayed on the bottom of the figure. The hatched region is the calculated transition region based on the thermal diffusivity obtained from the curve fit. The f_e for this sample is 0.60. In (a), the error from t^* to $4t^*$ range is virtually all negative while in (b) there is a significant period (shaded box) in which the error is nearly centered on zero.

The key difference is that for end fitting time at 10s (Figure 9(a)), the error oscillates above and below the zero line and there is no significant region where $T - T_{fit}$ is near zero. With this poor fit in the t* to 4t* region, the calculated f_{FT} is erroneous. For a 13 s end fitting time, about 50% of the time interval stable around the zero line (Figure 9(b)) and the results f_{FT} value is within 5% of the sample f_e.

(2) The sudden rise or fall of $T - T_{fit}$ near the end fitting time should be smaller than 0.01 K. If there is a rise and fall near the end fitting times, the peak should not be greater than 0.01 K. Sharp changes in $T - T_{fit}$ near the end of the fitting region indicate a systemic fitting error that will lead to an incorrect value of f_{FT} even when the error in the t^* to $4t^*$ is centered around zero as seen in Figure 10. Figure 10 shows a set of $T - T_{fit}$ for one 0.79 mm sample of the same flash with end fitting time at 17 s and 18 s.

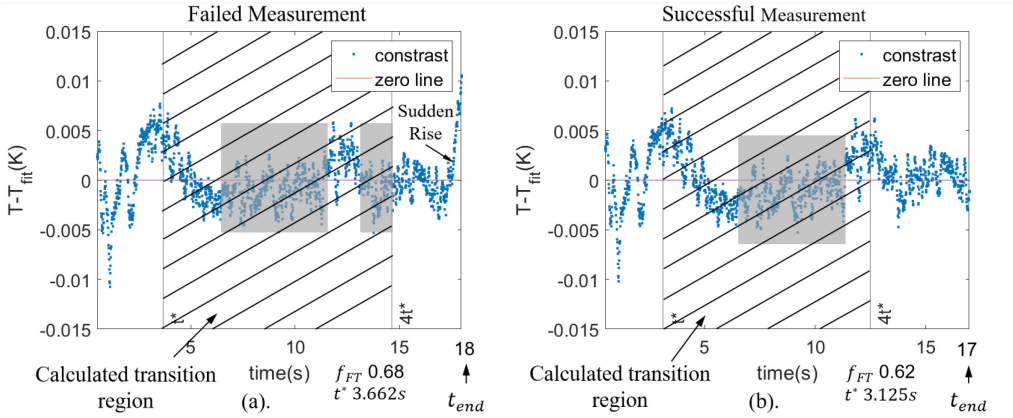

Figure 10. The $T - T_{fit}$ of one 0.79 mm sample of the same flash with different end fitting times, 1 s (a) and 17 s (b). t_{end} is end fitting time. The f_e of this sample is 0.60. The hatched region is the calculated transition region based on the thermal diffusivity obtained at the end fitting time. The rise of R_s at 18 s increases 10% on f_{FT} compared with the f_{FT} calculated for an end fitting time of 17 s. The shaded boxes show the data interval near zero. The sudden rise near the end fitting is marked in Figure 10(b).

In Figure 10(a), the calculated f_{FT} with the sudden rise of 0.01K in R_s at the end fitting time is 0.68 compared to f_e of 0.60. If this rise continues, the f_{FT} at longer end fitting times (19 s to 21 s) will continue to increase, because the percentage of high $T - T_{fit}$ time interval increases. However, at a shorter end fitting time, Figure 10(b), the fit error at the end of the fit region is low and the calculated density ($f_{FT} = 0.62$) is accurate ($f_e = 0.60$).

(3) The end fitting time needs to be at least $3t^*$ based on the obtained thermal diffusivity. This has been proven in the numerical model section.

(4) The t^* based on the obtained thermal diffusivity should be greater than the initial fitting time.

The quantity t^* represents a temporal moment near the turning point within the transitional stage depicted in Figure 3 (Shepard and Beemer, 2016). It is essential that the 't^*' value, derived from the obtained thermal diffusivity, is larger than the initial fitting time to assure that the key transition is included in the fitting range to assure the uniqueness of the fitting solution.

Experimental Results

Thermal Properties

Using the acceptance criteria detailed above, the 89 flashes of the six samples were processed and the unacceptable measurement results were removed. 40 out of 89 flashes were accepted (45%). For each flash, the calculated thermal properties and density (f_{FT}), for every end fitting time that meets the acceptability criteria is averaged to obtain a single data point per flash. The sample mean line denotes the average of these results from each flash of that sample.

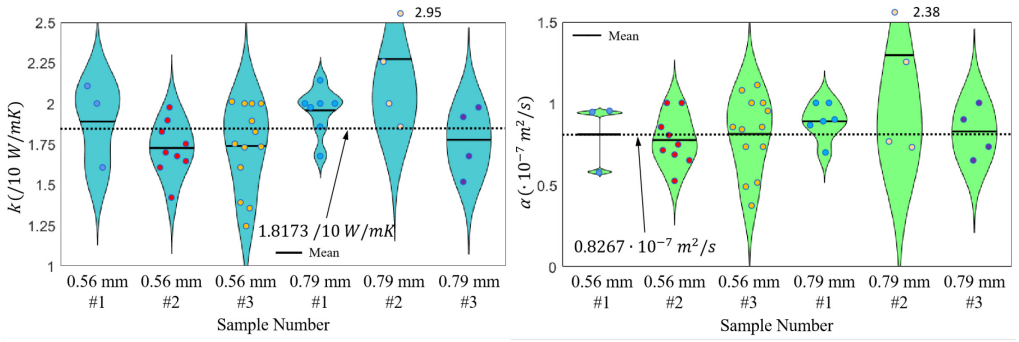

(a) (b)

Figure 11. The violin plot illustrating distribution of (a) thermal diffusivity and (b) thermal conductivity of the six testing samples. The points represent the value obtained from one flash. The points outside the y-axis for sample 0.79 mm #2 are from one problematic measurement. The two dashed lines are the overall sample average of the thermal properties excluding the 0.79 mm #2 sample.

Figure 11 shows the probability density distribution of the thermal properties using violin plot. The possibility density of the values is represented by width of the plots. The plot utilizes a kernel density estimator to create a smoothed curve based on the provided data. Excluding the failure measurements from 0.79 mm #2 discussed below, the overall average of thermal diffusivity and thermal conductivity for the sample average are $0.8267 \cdot 10^{-7}\ m^2/s$ and $0.1817\ W/mK$, respectively. The overall averages of the thermal diffusivity and thermal conductivity closely match

those obtained by lock-in thermography for SS304L powder from the work of Liu et al., which are $0.84 \cdot 10^{-7}\ m^2/s$ and $0.181\ W/mK$ (Liu et al., 2023). The relative density of the SS304L powder in this published work is 0.54. Given that SS304L and SS316L have nearly identical bulk thermal properties and the similar relative densities of the samples in this work and the literature, this suggests that the thermal properties determined by FT are credible (Alkahari et al., 2012, SANDVIK). Thus, FT can estimate the thermal properties of powder non-invasively.

While the average values appear reliable, the coefficient of variation (standard deviation divided by average) of the thermal diffusivity and thermal conductivity between flashes of one sample range from 19% to 29% and 8% to 15%, respectively (excluding 0.79 mm #2). To obtain an accurate estimate of the thermal properties of the sample, the sample needs to be flashed multiple times. Additional evidence of the accuracy of f_{FT} calculated from the thermal properties is obtained by comparing f_e and f_{FT} as discussed below.

Although multiple flashes are required to obtain accurate thermal properties of SS316L powder, the results are still useful because there are few measurements of these properties. The acquired thermal values can be used for improving the accuracy of melt pool simulation in powder bed fusion, by utilizing actual powder thermal properties rather than assuming the thermal conductivity of the powder is 1% of the bulk thermal conductivity (Zhang et al., 2019). Furthermore, this methodology can be applied to other powder materials. The powder bed thermal properties will also be helpful in understanding the binder curing process in BJ to optimize curing ties and may help in developing systematic ways of selecting appropriate interlayer drying parameters in BJ.

Of even greater use could be the ability to characterize the thermal properties of wet powders in BJ before curing. This is not feasible with current powder characterization methods but could be measured in situ by using SS316L dry powder as substrate to support the green body. When flashed, the properties of the green body could be found from the known thickness of the green body if the thermal properties of the dry powder are known. The thermal properties could even be correlated to the saturation level of the powder to help monitor the progress of binder drying during printing and curing after printing. The in-process drying has been shown to be critical to maintaining accurate part geometry in binder jetting (Crane, 2020).

Relative Density

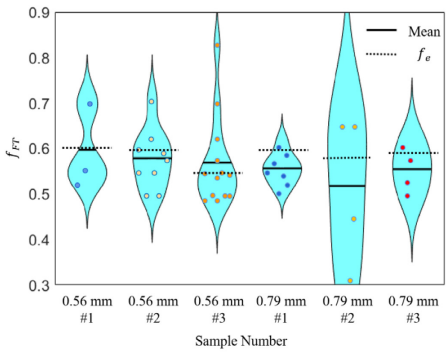

Figure 12. Violin plot of f_{FT} showcasing density values. The lines represent the average of f_{FT} for the sample, the density measured by weight (f_e). For 0.79 mm #2, the powder was disturbed while weighing and some powder was lost, so the average of f_e across all 0.79 mm samples was used instead of a sample-specific f_e value. To ensure a reliable f_{mean}, three other 0.79 mm samples were created and weighed, but weren't tested by FT.

The experimental density measurements are 58.1% - 60.6% for all but sample 0.56 mm #3 (55.1%). The low f_e of 0.56 mm #3 could be attributed to the repeatability issues of the BJ machine, blockages in the screen mesh, or errors in the first stratum thickness value. All of the sample means are within 8% of the experimental measurements. This low R_e value confirms the validity of the assumptions of the analytical model: surface absorption, absence of contact resistance, and a square-wave flash. Also, for 0.54 mm sample, the sample surface temperature is captured at both 100 Hz and 220 Hz. No improvements are found in the results that have higher frequencies. Therefore, 100 Hz seems sufficient to process capture the thermal properties and f_{FT} for SS 316L thicker than 0.54 mm.

The probability distribution of f_{FT} in Figure 12 shows significant scatter in f_{FT} results (the coefficient of variation ranges from 6.3% to 17.3%, expect for 0.79 mm #2 sample). This scatter arises from the influence of R_s on the time interval ranging from $1t^*$ to $4t^*$, which has a large impact on individual measurements but is substantially reduced by averaging multiple flashes. Unfortunately, the need to average multiple flashes hinders real-time monitoring of f_{FT} for the dry powder resting on SLA substrate using FT. While multiple flashes alone would be inconvenient, we also found it important to allow 20 minutes between flashes to minimize temperature gradients in the powder as dictated by Eq. (7).

A particular concern revolves around the sample 0.79 mm #2. Despite its 6.3% R_e value of the sample average f_{FT}, it exhibits a poorly convergent probability density in violin plot, a shortfall attributed to the insufficient number of valid flashes — defined as those conducted with an ambient temperature fluctuation below 0.3 K — to ensure reliable density estimations. The sample's measurements spanned two days, but only the five flashes from the first day met the acceptance criteria. The second day's seven results had to be discarded, because the air conditioning system in the laboratory malfunctioned causing an excessive fluctuation of room temperature. Among the five valid flashes, one met the acceptance criteria yet the obtained f_{FT} is 25% bigger/smaller than the f_e value of the sample. The possibility of having this type of failure is 2.2% (2/89). Normally, such anomalies can be offset with a greater number of valid flashes, as seen with sample 0.54 mm #3; however, this approach was unviable for the 0.79 mm #2 sample due to the limited data pool.

The results show that the flash method can obtain useful estimates of the density and the thermal properties of powder samples that are not possible with current measurement methods. FT offers a valuable approach for studying density variations across the powder bed with improved spatial resolution. By utilizing FT, the cumbersome steps of printing a cup structure and manually removing excess powder to determine powder bed density is unnecessary. This efficiency can also facilitate studies into the effects of different processing parameters on powder bed density.

However, two primary vulnerabilities of the approach are apparent: (1) sensitivity to R_s of just 0.005 K within the $1t^*$ to $4t^*$ time interval and (2) ambient temperature fluctuations must be < 0.3 K. These challenges stem from the nearly linear post-flash surface temperature profile as indicated in Figure 3 making it susceptible to environmental and equipment disturbances. Any sample with an E value nearing unity is very sensitive to temperature nonuniformity and noise in the temperature measurements making it challenging to use these methods for reliable single flash measurements. For successful online monitoring via FT, the E value of the sample system should not be too close to 1. Additionally, the impact of the R_s noise from the IR camera on the measurements should be minimized. However, FT holds potential for investigating the thermal properties and powder bed density of powders.

Conclusion

This research has shown that FT can non-invasively estimate the thermal properties and relative density (R_e of f_{FT} within 8%) of SS 316L powder when the powder rests on an SLA substrate. With this technique, powder density measurement with greater spatial resolution is possible. It can help identify sources of defects and density gradients in BJ parts for improved part quality. The thermal properties can enhance the simulation of melting pools in LPBF and predict required curing times in BJ parts. In situ thermal property measurement offers a pathway to better understand the relationship between saturation levels and the green body's thermal properties, potentially aiding in monitoring binder drying progress in BJ during both printing and post-processing. The density and saturation are critical to part quality but there are currently no methods to guide process development or assure process control.

Nevertheless, challenges persist. A primary concern emerges from the scatter in measurement results, underscored by a significant coefficient of variation. This scatter is largely attributed to the presence of systemic deviation in data (R_s) within the $1t^*$ to $4t^*$ time interval in the temperature data. Direct monitoring of f_e during the BJ printing process is made challenging when utilizing a dry powder on a substrate such as SLA polymer that has a similar value of effusivity ($\rho C_p k$) as the powder. Additionally, accurate measurements required many flashes with a long cooling interval between flashes. An additional challenge posed by the powder-on-SLA sample is the need for precise room temperature regulation within a narrow 0.3 K range. The root of these challenges is the *E* value of the sample system, which is close to one, leading to an almost linear transition stage. This linear post-flash behavior heightens the sensitivity to both the presence of R_s in the temperature data and fluctuations in room temperature. This should be improved by measuring f_{FT} on samples with *E* values distinctly different from 1. This aims to enhance the sample system's transition stage, making it resilient against R_s influences within the $1t^*$ to $4t^*$ time interval.

References

AISI Type 316L Stainless Steel, annealed sheet [Online]. Available: https://www.matweb.com/search/datasheet_print.aspx?matguid=1336be6d0c594b55afb5ca8bf1f3e042 [Accessed].

ALI, U., MAHMOODKHANI, Y., SHAHABAD, S. I., ESMAEILIZADEH, R., LIRAVI, F., SHEYDAEIAN, E., HUANG, K. Y., MARZBANRAD, E., VLASEA, M. & TOYSERKANI, E. 2018. On the measurement of relative powder-bed compaction density in powder-bed additive manufacturing processes. *Materials & Design,* 155**,** 495-501.

ALKAHARI, M. R., FURUMOTO, T., UEDA, T., HOSOKAWA, A., TANAKA, R. & ABDUL AZIZ, M. S. 2012. Thermal conductivity of metal powder and consolidated material fabricated via selective laser melting. *Key Engineering Materials,* 523**,** 244-249.

BALAGEAS, D. L., KRAPEZ, J.-C. & CIELO, P. 1986. Pulsed photothermal modeling of layered materials. *Journal of applied physics,* 59**,** 348-357.

CHEN, H., WEI, Q., WEN, S., LI, Z. & SHI, Y. 2017. Flow behavior of powder particles in layering process of selective laser melting: Numerical modeling and experimental verification based on discrete element method. *International Journal of Machine Tools and Manufacture,* 123**,** 146-159.

COLTON, T., LIECHTY, J., MCLEAN, A. & CRANE, N. 2021. Influence of drop velocity and droplet spacing on the equilibrium saturation level in binder jetting.

CRANE, N. B. 2020. Impact of part thickness and drying conditions on saturation limits in binder jet additive manufacturing. *Additive Manufacturing,* 33**,** 101127.

DEEMER, C. 1999. Front-flash thermal imaging characterization of continuous fiber ceramic composites. Argonne National Lab., IL (US).

EL RASSY, E. 2019. *Development of Methods to Identify Thermophysical Properties of Complex Media.* Chasseneuil-du-Poitou, Ecole nationale supérieure de mécanique et d ….

ELLIOTT, A. M., NANDWANA, P., SIDDEL, D. & COMPTON, B. A method for measuring powder bed density in binder jet additive manufacturing process and the powder feedstock characteristics influencing the powder bed density. 2016 International Solid Freeform Fabrication Symposium, 2016. University of Texas at Austin.

FARZADI, A., SOLATI-HASHJIN, M., ASADI-EYDIVAND, M. & ABU OSMAN, N. A. 2014. Effect of layer thickness and printing orientation on mechanical properties and dimensional accuracy of 3D printed porous samples for bone tissue engineering. *PloS one,* 9**,** e108252.

GAYTAN, S., CADENA, M., KARIM, H., DELFIN, D., LIN, Y., ESPALIN, D., MACDONALD, E. & WICKER, R. 2015. Fabrication of barium titanate by binder jetting additive manufacturing technology. *Ceramics International,* 41**,** 6610-6619.

HAERI, S., WANG, Y., GHITA, O. & SUN, J. 2017. Discrete element simulation and experimental study of powder spreading process in additive manufacturing. *Powder Technology,* 306**,** 45-54.

HAN, X., FAVRO, L., KUO, P. & THOMAS, R. 1996. Early-time pulse-echo thermal wave imaging. *Review of progress in quantitative nondestructive evaluation.* Springer.

KRUTH, J. P., MERCELIS, P., VAN VAERENBERGH, J., FROYEN, L. & ROMBOUTS, M. 2005. Binding mechanisms in selective laser sintering and selective laser melting. *Rapid prototyping journal,* 11**,** 26-36.

LI, M., DU, W., ELWANY, A., PEI, Z. & MA, C. 2020. Metal binder jetting additive manufacturing: a literature review. *Journal of Manufacturing Science and Engineering,* 142.

LIU, B., WILDMAN, R., TUCK, C., ASHCROFT, I. & HAGUE, R. Investigation the effect of particle size distribution on processing parameters optimisation in selective laser melting process. 2011 International Solid Freeform Fabrication Symposium, 2011. University of Texas at Austin.

LIU, T., KINZEL, E. C. & LEU, M. C. 2023. In-situ lock-in thermographic measurement of powder layer thermal diffusivity and thickness in laser powder bed fusion. *Additive Manufacturing,* 74**,** 103726.

MALDAGUE, X. 1996. Nondestructive evaluation of materials by infrared thermography. *NDT and E International,* 6**,** 396.

MIYANAJI, H., RAHMAN, K. M., DA, M. & WILLIAMS, C. B. 2020. Effect of fine powder particles on quality of binder jetting parts. *Additive Manufacturing,* 36**,** 101587.

MOSTAFAEI, A., ELLIOTT, A. M., BARNES, J. E., LI, F., TAN, W., CRAMER, C. L., NANDWANA, P. & CHMIELUS, M. 2021. Binder jet 3D printing—Process parameters, materials, properties, modeling, and challenges. *Progress in Materials Science,* 119**,** 100707.

MUZIKA, L., ŠVANTNER, M., HOUDKOVá, Š. & ŠULCOVá, P. 2021. Application of flash-pulse thermography methods for quantitative thickness inspection of coatings made by different thermal spraying technologies. *Surface and Coatings Technology,* 406**,** 126748.

PARKER, W., JENKINS, R., BUTLER, C. & ABBOTT, G. 1961. Flash method of determining thermal diffusivity, heat capacity, and thermal conductivity. *Journal of applied physics,* 32**,** 1679-1684.

PIERCE, J. & CRANE, N. B. 2019. Impact of Pulse Length on the Accuracy of Defect Depth Measurements in Pulse Thermography. *Journal of Heat Transfer,* 141.

RAJIC, N. 2013. Non-destructive evaluation (NDE) of aerospace composites: Flaw characterisation. *Non-Destructive Evaluation (NDE) of Polymer Matrix Composites.* Elsevier.

RINGERMACHER, H. I., ARCHACKI JR, R. J. & VERONESI, W. A. 1998. Nondestructive testing: transient depth thermography. Google Patents.

SANDVIK. *OSPREY® 316L FOR ADDITIVE MANUFACTURING* [Online]. Available: https://www.metalpowder.sandvik/siteassets/metal-powder/datasheets/osprey-316l-am-austenitic-stainless-steels.pdf [Accessed].

SHEPARD, S. M. & BEEMER, M. F. Multilayer material characterization using thermographic signal reconstruction. AIP Conference Proceedings, 2016. AIP Publishing LLC, 100005.

SHEPARD, S. M., LHOTA, J. R., RUBADEUX, B. A., WANG, D. & AHMED, T. 2003. Reconstruction and enhancement of active thermographic image sequences. *Optical Engineering,* 42**,** 1337-1342.

SOLUTIONS, M. 2014. *EOS M 290： The Additive Manufacturing System for the Production of Serial Components, Spare Parts and Functional Prototypes Directly in Metal.* [Online]. Available: https://engineering.cmu.edu/next/_files/documents/eos-m-290-description.pdf [Accessed].

SUN, J. 2003. Method for determining defect depth using thermal imaging. Univ. of Chicago, IL (United States).

SUN, J. 2006. Analysis of pulsed thermography methods for defect depth prediction. *Journal of Heat Transfer,* 128**,** 329-339.

SUN, J. 2010. Method for analyzing multi-layer materials from one-sided pulsed thermal imaging. Google Patents.

SUN, J. 2014. Pulsed thermal imaging measurement of thermal properties for thermal barrier coatings based on a multilayer heat transfer model. *Journal of heat transfer,* 136**,** 081601.

TECHNOLOGIES, A. C. F. O. A. M. & TERMINOLOGY, A. C. F. O. A. M. T. S. F. O. 2012. *Standard terminology for additive manufacturing technologies*, Astm International.

UTELA, B., STORTI, D., ANDERSON, R. & GANTER, M. 2008. A review of process development steps for new material systems in three dimensional printing (3DP). *Journal of Manufacturing Processes,* 10**,** 96-104.

WALLACE, N. J., CRANE, N. B. & JONES, M. R. 2022. Defect measurement limits using flash thermography with application to additive manufacturing. *NDT & E International,* 128**,** 102615.

WHEAT, E., VLASEA, M., HINEBAUGH, J. & METCALFE, C. 2018. Sinter structure analysis of titanium structures fabricated via binder jetting additive manufacturing. *Materials & Design,* 156**,** 167-183.

WYSOCKA-FOTEK, O., OLIFERUK, W. & MAJ, M. 2012. Reconstruction of size and depth of simulated defects in austenitic steel plate using pulsed infrared thermography. *Infrared Physics & Technology,* 55**,** 363-367.

ZHANG, Z., HUANG, Y., KASINATHAN, A. R., SHAHABAD, S. I., ALI, U., MAHMOODKHANI, Y. & TOYSERKANI, E. 2019. 3-Dimensional heat transfer modeling for laser powder-bed fusion additive manufacturing with volumetric heat sources based on varied thermal conductivity and absorptivity. *Optics & Laser Technology,* 109**,** 297-312.

ZHENG, K., CHANG, Y.-S., WANG, K.-H. & YAO, Y. 2015. Improved non-destructive testing of carbon fiber reinforced polymer (CFRP) composites using pulsed thermograph. *Polymer Testing,* 46**,** 26-32.

ZIAEE, M. & CRANE, N. B. 2019. Binder jetting: A review of process, materials, and methods. *Additive Manufacturing,* 28**,** 781-801.

ZIAEE, M., TRIDAS, E. M. & CRANE, N. B. 2017. Binder-jet printing of fine stainless steel powder with varied final density. *Jom,* 69**,** 592-596.